



**HAL**  
open science

# Late Carboniferous paleoelevation of the Variscan Belt of Western Europe

Camille Dusséaux, Aude Gébelin, Gilles Ruffet, Andreas Mulch

► **To cite this version:**

Camille Dusséaux, Aude Gébelin, Gilles Ruffet, Andreas Mulch. Late Carboniferous paleoelevation of the Variscan Belt of Western Europe. *Earth and Planetary Science Letters*, 2021, 569, pp.117064. 10.1016/j.epsl.2021.117064 . insu-03277747

**HAL Id: insu-03277747**

**<https://insu.hal.science/insu-03277747v1>**

Submitted on 5 Jul 2021

**HAL** is a multi-disciplinary open access archive for the deposit and dissemination of scientific research documents, whether they are published or not. The documents may come from teaching and research institutions in France or abroad, or from public or private research centers.

L'archive ouverte pluridisciplinaire **HAL**, est destinée au dépôt et à la diffusion de documents scientifiques de niveau recherche, publiés ou non, émanant des établissements d'enseignement et de recherche français ou étrangers, des laboratoires publics ou privés.



33 suggests that the hinterland of the Variscan belt of western Europe was high enough to  
34 act as a barrier to moisture transport from the south-south-east and induce an orographic  
35 rain shadow to the north.

## 36 **Keywords**

37 Stable isotope paleoaltimetry; meteoric fluids; shear zone; detachment; basin; Variscan;  
38 Carboniferous.

## 39 **1. Introduction**

40 The Variscan belt, extending from South America to East Asia through North America  
41 and Central Europe, is a Himalayan-type collision belt that resulted from protracted  
42 convergence between the Laurentia-Baltica and Gondwana lithospheric plates between  
43 ~410 and ~310 Ma (e.g. Matte, 2001). This extensive mountain belt exposes vast  
44 amounts of granites, migmatitic complexes and granulite facies rocks and is considered  
45 a “hot orogen” characterized by crustal thickening, syntectonic crustal melting, high-  
46 grade metamorphism, and syn- to post-convergence gravitational collapse (Fig. 1; e.g.  
47 G ebelin et al., 2009; Vanderhaeghe et al., 2020).

48 The paleotopography of the Variscan orogen has been the focus of considerable debate  
49 with estimates ranging from ~2000 to ~5000 m (e.g. D orr and Zulauf, 2010; Franke,  
50 2014). Principally, two competing models have been proposed: 1) a Himalaya-Tibet style  
51 high orogenic plateau that developed as a result of thickened hinterland regions (e.g.  
52 Becq-Giraudon et al., 1996; D orr and Zulauf, 2010; Godd eris et al., 2017), and 2)  
53 subdued topography due to coeval orogen-parallel extension that counterbalanced  
54 crustal thickening and surface uplift (e.g. Roscher and Schneider, 2006; Franke, 2014).  
55 Therefore, assessing the paleoaltitude of this mountain chain is critical to distinguish  
56 between these two models.

57 Quantifying the topographic evolution of the Variscan belt is also of capital importance  
58 to understanding its impact on past global climate change as the Late Carboniferous-  
59 Permian transition represents a period of climatic upheaval (Monta nez and Poulsen,  
60 2013). By analogy with the modern Himalayan-Tibetan orogen strengthening the modern

61 Asian Monsoon climate (Boos and Kuang, 2010), global and local climate variability  
62 would have been majorly impacted by the elevation changes of the Central Pangean  
63 (Appalachian-Variscan) mountain belt (e.g. Fluteau et al., 2001). However, no  
64 quantification of Paleozoic surface topography has been obtained to date for the  
65 Variscan orogen.

66 Here, we use stable isotope paleoaltimetry, a technique that recovers the isotopic  
67 composition of ancient rainwater which scales in a predictable fashion with elevation  
68 (e.g. Poage and Chamberlain, 2001), with the aim of quantifying paleoelevation of the  
69 hinterland of the Variscan belt of Western Europe during the Late Carboniferous.  
70 However, assessing paleoelevation of this fully eroded mountain belt is challenging  
71 because the proxies commonly used to reconstruct the topography of orogens (e.g.  
72 lacustrine and pedogenic carbonates, volcanic glasses) are absent or altered. Here, we  
73 present the first paleoaltimetry estimates for the Variscan belt based on the hydrogen  
74 isotope ratios of ancient precipitation retrieved from the low  $\delta D$  values of synkinematic  
75 muscovite ( $\delta D_{Ms} \leq -90\text{‰}$ ) that crystallized at  $\sim 315$  Ma in the footwall of extensional shear  
76 zones in the continental interior of the orogen.

## 77 **2. Methods**

### 78 **2.1. Stable isotope paleoaltimetry of eroded orogens**

79  $\delta D$  values of meteoric fluids can be retrieved from minerals that crystallize during high-  
80 temperature deformation in active shear zones infiltrated by surface fluids. Shear zone-  
81 based paleoaltimetry has been applied to reconstruct the topography of the Cenozoic  
82 western United States (e.g. Mulch et al., 2007; Gébelin et al., 2012) and the Miocene  
83 Himalaya (Gébelin et al., 2013). It is based on the concept that hydrous (shear zone)  
84 minerals crystallize in equilibrium with surface-derived, meteoric water. In this study, we  
85 use muscovite as a paleoaltimetry proxy because of its 1) high resistance to post-  
86 deformational alteration and low-temperature hydrogen isotope exchange, and 2) ability  
87 to directly record the timing of mineral formation and isotopic exchange through e.g.  
88  $^{40}\text{Ar}/^{39}\text{Ar}$  geochronology (e.g. Mulch et al., 2005). However,  $\delta D$  values extracted from

89 synkinematic silicates represent maximum values for meteoric fluids, thus minimum  
90 paleoelevation estimates, because fluid compositions may be shifted to less negative  
91 values at depth due to fluid-rock interaction that occurs during the downward flow of  
92 fluids (e.g. Taylor, 1977; Gébelin et al., 2012, 2013). As shown in previous studies of  
93 extensional detachment systems, penetration of surface-derived fluids down to the  
94 brittle-ductile transition is typically supported by the presence of a large hydraulic head,  
95 a porous and permeable upper crust, and a high heat flux sourced by granite and  
96 migmatite emplacement in the middle and lower crust, essential to sustain fluid  
97 circulation within the top of the active detachment footwall (e.g. Person et al., 2007;  
98 Gébelin et al., 2015, 2017; Dusséaux et al., 2019).

99 Single-site paleoaltimetry reconstructions suffer from uncertainties around paleoclimatic  
100 boundary conditions, especially in deep time applications. One approach to resolve  
101 climatically induced biases in stable isotope paleoaltimetry (Mulch, 2016, and references  
102 therein) is to compare high-elevation stable isotope records (herein from the hinterland  
103 of the Variscan belt of western Europe) to climate-controlled records near sea level  
104 (herein fresh-water shark remains).

## 105 **2.2. Retrieving the isotope composition of meteoric water in the hinterland**

### 106 **2.2.1. Sampling strategy**

107 Syntectonic leucogranites were first sampled at regional scale within strike-slip and  
108 detachment shear zones to determine the overall pattern of fluid compositions from the  
109 hydrogen isotope ratio of muscovite ( $\delta D_{Ms}$ ; Fig. 2). Based on preliminary results ( $\delta D_{Ms}$   
110 values  $< -90\text{‰}$ ), specific sites were subsequently targeted to gain a representative range  
111 of hydrogen isotopic compositions for the meteoric fluids that permeated these shear  
112 zones.

113 Samples from detachment zones were collected based on their structural position from  
114 the hanging wall/footwall interface into the mylonitic footwall. Poor outcrop conditions  
115 precluded observation of the hanging wall contact and samples were instead collected  
116 most proximally to the detachment interface. Additional sample collection included  
117 micaschist and orthogneiss (from the host rocks), as well as pegmatites and muscovite-

118 rich quartz veins (either found parallel to the granite foliation, filling brittle fractures and/or  
119 lining fault surfaces that formed in the hanging wall, Fig 3).

120 For the stable isotope paleoaltimetry reconstruction, we focused on samples from the  
121 northeast corner of the Millevaches massif where especially low  $\delta D_{Ms}$  values provide  
122 strong evidence for interaction with meteoric fluids. We particularly targeted the low-  
123 angle Felletin detachment zone that forms the roof of the leucogranites (Fig. 2A).

#### 124 **2.2.2. Structural and petrostructural analysis**

125 Structural features, including measurements of foliation planes and lineation direction,  
126 were described in detail from a continuous section (Fig. 3A) into the mylonitic footwall of  
127 the Felletin detachment shear zone, from mylonitic leucogranite at the top (MIL19 – 0m)  
128 to undeformed leucogranite at the bottom (MIL18I – 90m). Thin sections were  
129 systematically cut parallel to the lineation and perpendicular to the foliation to determine  
130 the sense of shear. Micromorphological investigations of muscovite microstructures were  
131 performed to characterize the mechanisms of deformation and fluid flow history.

#### 132 **2.2.3. Hydrogen isotope geochemistry**

133 To determine the isotopic composition of meteoric fluids that penetrated the Felletin  
134 detachment footwall, we 1) measured the hydrogen isotope ratios of muscovite (Text  
135 SM1; Table SM1), 2) deduced an average temperature of hydrogen isotope exchange  
136 using the titanium-in-muscovite geothermometer (Text SM2, Table SM2; Wu and Chen,  
137 2015), and 3) used the hydrogen isotope muscovite-water fractionation factor of Suzuoki  
138 and Epstein (1976) (Table 1).

#### 139 **2.2.4. Ar/Ar geochronology**

140 To constrain the timing and duration of recrystallization and fluid flow in the hydrothermal  
141 system, five muscovite single grains from mylonitic leucogranite samples MIL19,  
142 MIL18C, MIL18D, MIL18H and MIL18I were laser step-heated for  $^{40}\text{Ar}/^{39}\text{Ar}$   
143 geochronology (Fig. 3D; Text SM3; Tables SM3 and SM4).

144 **2.3. Retrieving the isotope composition of meteoric water in the low-elevation**  
145 **foreland: The Bourbon l'Archambault basin**

146 For our stable isotope paleoaltimetry reconstruction, we reference the hydrogen isotope  
147 record from the elevated Variscan hinterland (new data herein) to low-elevation oxygen  
148 isotope records from teeth and spines of two freshwater shark species preserved in the  
149 Bourbon l'Archambault basin (Fischer et al., 2013; Fig. 1B, Fig. SM2, Table 2). The  
150 phosphate-oxygen bond in shark teeth fluorapatite is very resistant to diagenetic  
151 alteration, thus representing a reliable low-elevation proxy. The Bourbon l'Archambault  
152 basin is situated close to our study area (~100 km from the hinterland sites) and  
153 developed close to sea level in the external zones of the orogen (Fischer et al., 2013).  
154 Sedimentological, paleogeographical, ecological and geochemical ( $\delta^{18}\text{O}_\text{P}$  and  $^{87}\text{Sr}/^{86}\text{Sr}$   
155 values; Table 2) data from previous studies indicate that the sharks evolved in a  
156 freshwater environment (lacustrine to fluvial; Fischer et al., 2013). The sedimentary  
157 record has been biostratigraphically and isotopically dated as Sakmarian in age (~295  
158 to 290 Ma; e.g. Roscher and Schneider, 2005), and shark teeth have not been affected  
159 by diagenetic alteration resulting in well preserved bioapatite (Fischer et al., 2013). Nine  
160 *Lissodus* and seven *Orthacanthus* spines provide  $\delta^{18}\text{O}_\text{P}$  values that range from 15.5 to  
161 17.6‰ (n = 17) and  $^{87}\text{Sr}/^{86}\text{Sr}$  ratios from 0.71058 to 0.71077 (n=4). Data from these  
162 lifelong proxies are similar to those obtained on *Orthacanthus* tooth enameloid that yields  
163 a  $\delta^{18}\text{O}_\text{P}$  value of 16.6‰ and an  $^{87}\text{Sr}/^{86}\text{Sr}$  ratio of 0.71061.

164 **2.4. Lapse rate used for paleoaltimetry reconstructions**

165 In contrast to most stable isotope paleoaltimetry studies conducted in ancient orogens  
166 located in mid to low latitudes, our study focuses on an eroded mountain chain for which  
167 paleomagnetic data (e.g. Edel et al., 2018) indicate that it straddled the Equator during  
168 the Carboniferous (Fig. 1; e.g. Domeier and Torsvik, 2014; Kent and Muttoni, 2020).  
169 Here, we use the empirical isotope-elevation relationship (Poage and Chamberlain,  
170 2001) for global low-to-mid latitude mountain belts in order to estimate a Variscan  
171 paleoelevation.

172 However, this relationship between elevation and the  $\delta D$  and  $\delta^{18}O$  values of precipitation  
173 must be applied with caution. When comparing with present-day conditions, three  
174 parameters may have changed the isotopic lapse rate over the Pangean mountains  
175 during the late Carboniferous. The presence of an Intertropical Convergence Zone,  
176 typical of tropical regions, may have caused monsoonal precipitation and rising air  
177 masses, and, by controlling the spatiotemporal distribution of precipitation and  
178 consequently the isotopic composition, may have led to a reduced lapse rate when  
179 compared to higher latitudes (e.g. Poulsen et al., 2007; Heavens et al., 2015). Two  
180 important glacial periods at ~315 and ~295 Ma concomitant with the timing of proxy  
181 formation suggests that the Pangean domain was likely characterized by rather cold and  
182 arid conditions. When compared to modern observations, globally cooled conditions may  
183 have increased the lapse rate over high altitudes (~5000 m; e.g. Poage and  
184 Chamberlain, 2001; Heavens et al., 2015; Kent and Muttoni, 2020). Global temperatures  
185 during the Late Carboniferous may have been up to 10°C cooler than modern  
186 temperatures (Feulner, 2017). Hence, simple Rayleigh distillation under glacial  
187 temperatures is expected to result in lower paleoaltitude estimates; an effect that may  
188 account for lowering of calculated paleoelevations on the order of 5-20 % (Rowley,  
189 2007).

190 Here, we calculate paleoelevation of the Variscan belt of Western Europe using a lapse  
191 rate defined for mid to low latitudes (-2.8‰/km for  $\delta^{18}O$  and -22‰/km for  $\delta D$ ; Poage and  
192 Chamberlain, 2001). However, considering the equatorial paleogeographic context, this  
193 lapse rate underestimates paleoaltimetry estimates when compared to present-day  
194 tropical lapse rates (-1.8‰/km for  $\delta^{18}O$  and -14.6‰/km for  $\delta D$ ; Saylor et al., 2009).

### 195 **3. Hinterland data: western part of the French Massif Central**

#### 196 **3.1. Geological background**

197 The focus of this study is on the Limousin region (Western part of the French Massif  
198 Central) where syntectonic granites are spatially associated with major detachment and  
199 strike-slip shear zones. The Limousin is part of the hinterland of the West European

200 Variscan collisional belt that shows a range of tectono-metamorphic events (~360 - 310  
201 Ma) from crustal thickening and associated Barrovian metamorphism to lithospheric  
202 thinning accommodated by regional-scale strike-slip shear zones and low-angle  
203 detachment zones (e.g. Matte, 2001; G ebelin et al., 2009; Vanderhaeghe et al., 2020).  
204 Here, the end of the orogeny (~320 to 300 Ma) is characterized by high-grade  
205 metamorphism and syntectonic leucogranites emplacement within crustal-scale shear  
206 zones distributed in a flower structure representing the south-east extension of the South  
207 Armorican Shear Zone (Fig. 2A; G ebelin et al., 2007, 2009). These Late Carboniferous  
208 shear zones were active while this part of the orogen was otherwise collapsing, inducing  
209 the development of extensional structures in the internal transpression zones and thrust  
210 faults in the external zones (e.g. G ebelin et al., 2007, 2009).

### 211 **3.2. Stable isotope results at the regional scale**

212 Samples (n=68) of leucogranite, pegmatite, quartz vein, micaschist, and gneiss from  
213 ductile shear zones yield muscovite hydrogen isotope ratios ( $\delta D_{Ms}$ ) between  $-116 \pm 2\text{‰}$   
214 to  $-40 \pm 2\text{‰}$  (Fig. 2; Table SM1). Muscovite from mylonitic leucogranites emplaced within  
215 strike-slip shear zones in the northern part of the area (La Marche shear zone) provide  
216  $\delta D_{Ms}$  values ranging from  $-87$  to  $-80\text{‰}$  (n=2). In contrast, muscovite from deformed  
217 leucogranite further south along the St-Michel-de-Veisse (n=11) and La Courtine (n=2)  
218 dextral strike-slip faults provides lower  $\delta D_{Ms}$  values from  $-107$  to  $-76\text{‰}$ . However,  
219 undeformed leucogranites from this southern strike-slip fault network show higher values  
220 of  $-74\text{‰}$  and  $-72\text{‰}$  (n=2). Sheared pegmatites from the same strike-slip shear zones  
221 indicate consistently low  $\delta D_{Ms}$  values between  $-102$  and  $-76\text{‰}$  (n=12), while quartz veins  
222 (n=4) yield constant  $\delta D_{Ms}$  values that range from  $-87$  to  $-82\text{‰}$ . Higher  $\delta D_{Ms}$  values ( $-79$   
223 to  $-66\text{‰}$ ; n=4) have been measured on syntectonic muscovite from the strike-slip  
224 Pradines mylonitic fault in the Millevaches massif.

225 Perpendicular to the E-W strike-slip shear zone trend, low-angle normal faults bound the  
226 Br ame massif (northwest corner of the Limousin region) and the Millevaches massif. The  
227 Nantiat detachment that forms the western boundary of the Br ame massif, exposes  
228 mylonitic granites that yield  $\delta D_{Ms}$  values ranging from  $-73$  to  $-55\text{‰}$  (n=2). Lower  $\delta D_{Ms}$

229 values from -84 to -74‰ (n=3) are found in the eastern part of the Brême massif along  
230 the Bussièrès-Madeleine normal fault. The brittle-ductile Argentat normal fault bounds  
231 the Millevaches massif to the west and indicates high  $\delta D_{Ms}$  values both in the hanging  
232 wall ( $-83‰ \leq \delta D_{Ms} \leq -49‰$  in 8 orthogneiss samples) and the footwall ( $-49‰ \leq \delta D_{Ms} \leq -$   
233  $40‰$  in 4 mica schist samples).

234 Much lower  $\delta D_{Ms}$  values ( $-116‰ \leq \delta D_{Ms} \leq -94‰$ ) are found in mylonitic leucogranite  
235 (n=9), undeformed leucogranite (n=1), mylonitic pegmatite (n=1) and a quartz vein (n=1)  
236 near Felletin (eastern Millevaches massif), at the junction of several brittle (Creuse and  
237 Felletin-Ambrugeat) and ductile (St-Michel-de-Veisse and Courtine) fault systems. To  
238 the northeast part of the Millevaches granite, brittle normal faults, part of the Felletin-  
239 Ambrugeat Fault system, have been sealed by muscovite-rich quartz veins that yield  
240  $\delta D_{Ms}$  values of -87 to -85‰ (MIL13A; Fig. 3E).

241 In the following, we focus on the Felletin detachment footwall where synkinematic  
242 muscovite highlight a strong meteoric fluid signature ( $\delta D_{Ms}$  values as low as -116‰; see  
243 discussion).

### 244 **3.3. Structural outcrop data**

245 Within the top ~80m of section in the Felletin mylonitic footwall, deformed two-mica  
246 leucogranites display a shallow to moderate (10-30°) ENE-dipping foliation (S plane) and  
247 a ~N025 trending stretching lineation. Syntectonic pegmatites (MIL18H) and quartz veins  
248 (MIL18F) are orientated parallel to the mylonitic leucogranite foliation. This foliation is  
249 characterized by S-planes making an angle of ~40° with C-planes marked by muscovite  
250 fish. C-S structures at the macroscopic (Fig. 3A-2) and microscopic scale (Fig. 3B-2)  
251 largely support a syntectonic leucogranite emplacement with a top-to-the-northeast  
252 sense of shear. Top-to-the-southwest sense of shear (indicated by asymmetric feldspar  
253 grains with pressure shadows) are also displayed in some samples. Nonetheless, the  
254 majority of shear sense indicators such as asymmetric tails and/or shear bands indicate  
255 a top-to-the-northeast sense of shear (Figs. 3A-2 and 3B-2).

256 The entire section is affected by extensional conjugate brittle fractures (Fig. 3A, red  
257 arrows) that, as observed to the north along the Felletin-Ambrugeat fault system, dip

258 ~50° to the ENE and WSW. Along the St Michel-de-Veisse fault (north of the section),  
259 similar fractures are filled by quartz veins containing muscovite (Fig. 3E).

### 260 **3.5. Petrostructural analysis**

261 Microstructural observations indicate an abundance of mica fish formed by simultaneous  
262 grain rotation and reduction of their upper and lower sides and drag along micro shear  
263 zones (Fig. 3B-1). Some ultramylonitic facies only show shear bands made of tiny grains  
264 that develop as a result of intense shearing and alteration of primary muscovite (Fig. 3B-  
265 3). In all studied samples (MIL19 – 0 m, MIL18C – 15 m, MIL18H – 60 m and MIL18I –  
266 90 m), quartz grains show sub-solidus deformation textures such as castellate  
267 microstructures indicating that grain boundary migration (~500 to 700°C; e.g. Stipp et al.,  
268 2002) was the dominant dynamic recrystallization process occurring during syntectonic  
269 granite emplacement (Fig. 3B-1 and 2). However sub-grain rotation operating at lower  
270 temperature (~400 to 500°C; e.g. Stipp et al., 2002) is also indicated by quartz ribbons  
271 of sheared pegmatite with low  $\delta D_{Ms}$  values (MIL18H,  $\delta D_{Ms} = -116\text{‰}$ ; Fig. 3B-3). In  
272 contrast, the undeformed granite sample (MIL18I) displays euhedral muscovite grains  
273 (Fig. 3B-4) and primary quartz crystals.

### 274 **3.6. Titanium-in-muscovite thermometry**

275 Three samples have been selected (mylonitic pegmatite MIL18H,  $\delta D_{Ms} = -116\text{‰}$ ;  
276 mylonitic leucogranite MIL18C,  $\delta D_{Ms} = -104\text{‰}$ ; and undeformed leucogranite MIL18I,  
277  $\delta D_{Ms} = -96\text{‰}$ ) covering a rather large deformation and strain gradient.

278 Muscovite grains contain  $0.00 < Ti < 0.05$  a.p.f.u,  $0.02 < Na < 0.10$  a.p.f.u,  $0.04 < Mg <$   
279  $0.18$  a.p.f.u and  $0.08 < Fe < 0.37$  a.p.f.u (Table SM2; Fig. SM1). Compositional profiles  
280 indicate chemical zoning of muscovite fish from the inner to the outer part of the grain  
281 highlighted by major element compositions and particularly evident for Mg, Fe and Na.  
282 From core to rim, we note an increase of up to three times in the Mg content (sample  
283 MIL18C zone B; core: Mg = 0.06 a.p.f.u; rim: Mg = 0.18 a.p.f.u) and four times in the Fe  
284 content (core: 0.08 a.p.f.u; rim: 0.37 a.p.f.u), and a decrease of up to eight times in the  
285 Na content (core: 0.10 a.p.f.u; rim: 0.02 a.p.f.u). Euhedral muscovite grains from the  
286 undeformed sample MIL18I do not show any particular compositional zonation and

287 display the same low-Mg ( $0.07 < \text{Mg} < 0.11$  a.p.f.u), low-Fe ( $0.08 < \text{Fe} < 0.12$  a.p.f.u)  
288 and high-Na ( $0.05 < \text{Na} < 0.09$  a.p.f.u) composition as the core of muscovite fish in  
289 deformed samples.

290 Using a pressure of  $4 \pm 1$  kbar (Gébelin et al., 2006) and the average chemical  
291 composition of muscovite for each individual sample, the geothermometer of Wu and  
292 Chen (2015) indicates temperatures of  $493 \pm 57^\circ\text{C}$  for the mylonitic leucogranite  
293 (MIL18C),  $568 \pm 42^\circ\text{C}$  for the pegmatite (MIL18H) and  $559 \pm 55^\circ\text{C}$  for the undeformed  
294 granite (MIL18I) yielding an average temperature of  $540 \pm 51^\circ\text{C}$  (Table SM2).

### 295 **3.7. Hydrogen isotopic composition of fluids in the Felletin footwall**

296 We calculated an average  $\delta\text{D}_{\text{water}}$  value of  $-96 \pm 8\text{‰}$  using a temperature of hydrogen  
297 isotope exchange of  $540 \pm 51^\circ\text{C}$ , the hydrogen isotope muscovite-water fractionation  
298 factor of Suzuoki and Epstein (1976) and the average of the lowest 30% of the measured  
299  $\delta\text{D}_{\text{Ms}}$  values ( $n=3$ ; MIL18H,  $\delta\text{D}_{\text{Ms}} = -116\text{‰}$ ; MIL19,  $\delta\text{D}_{\text{Ms}} = -109\text{‰}$ ; MIL18D,  $\delta\text{D}_{\text{Ms}} = -$   
300  $105\text{‰}$ ; see Figs. 4A and 4C, Table 1 and discussion below for details and uncertainties).

### 301 **3.8. $^{40}\text{Ar}/^{39}\text{Ar}$ Geochronology**

302 Muscovite from the MIL19 (0 m), MIL18C (15 m) and MIL18D (25 m) mylonitic  
303 leucogranite samples (Fig. 3D) provide plateau ages ( $1\sigma$ ) of  $316.7 \pm 0.7$  Ma,  $313.7 \pm 0.6$   
304 Ma, and  $314.0 \pm 0.6$  Ma, respectively, including more than 90% of total  $^{39}\text{Ar}_K$  released.  
305 The undeformed sample MIL18I (90 m) yields a plateau age of  $314.6 \pm 0.7$  Ma ( $1\sigma$ ). A  
306 muscovite from the MIL18H syntectonic pegmatite yields a saddle-shaped age spectrum  
307 with apparent ages from  $318.4 \pm 1.4$  to  $309.7 \pm 2.3$  Ma. In addition, a single muscovite  
308 grain from a brittle fault plane that developed in the hanging-wall provides a plateau age  
309 of  $313.8 \pm 0.7$  Ma ( $1\sigma$ ) (MIL13A, Fig. 3E).

## 310 **4. Discussion**

### 311 **4.1. Meteoric water-rock interaction in the Felletin detachment footwall**

312 Hydrogen isotope results from the Limousin region reveal a  $76\text{‰}$  difference in  $\delta\text{D}_{\text{Ms}}$   
313 values from values as high as  $-40\text{‰}$  indicating a deeper crustal (magmatic/metamorphic)  
314 origin ( $-80\text{‰} < \delta\text{D}_{\text{magmatic fluids}} < -40\text{‰}$  and/or  $-70\text{‰} < \delta\text{D}_{\text{metamorphic fluids}} < -20\text{‰}$ ; e.g. Field

315 and Fifarek, 1985) to values as low as -116‰ that undeniably reflect a signature of  
316 meteoric fluids sourced in either high elevation or high latitude areas (e.g. Mulch, 2016).  
317 Intermediate values are interpreted to reflect different degrees of mixing between these  
318 two fluid end members. A mixing relationship between meteoric and magmatic/  
319 metamorphic fluids has been already established in the southern Armorican domain  
320 based on a 42‰ difference ( $-88‰ \leq \delta D_{Ms} \leq -46‰$ ) amongst  $\delta D_{Ms}$  values extracted from  
321 Variscan mylonite collected from deep to shallow crustal levels (Dusséaux et al., 2019).  
322 The lowest calculated  $\delta D_{water}$  values ( $-104‰$  to  $-82‰ \pm 5‰$ ) were obtained in the Felletin  
323 detachment footwall (northeast corner of the Millevaches massif). We consider this to  
324 represent an exhumed, ancient hydrothermal system that was active during the Late  
325 Carboniferous. The structural setting - at the junction between major ductile and brittle  
326 fault systems - provides the opportunity for protracted pathways for the downward  
327 penetration of surface-derived fluids to the brittle-ductile transition.

328 D-depleted mica fish along shearing planes interacted with meteoric fluids during high  
329 temperature deformation as indicated by quartz microstructures ( $\sim 400$  to  $700^\circ\text{C}$ ; Fig. 3B)  
330 and the titanium-in-muscovite thermometer ( $540 \pm 51^\circ\text{C}$ ; Table SM2, Fig. SM1). This  
331 dataset agrees with previous electron backscatter diffraction (EBSD) data obtained on  
332 recrystallized quartz ribbons from similar samples that revealed plastic deformation  
333 dominated by prismatic  $\langle a \rangle$  glide which occurs between  $400$  and  $700^\circ\text{C}$  (Gébelin et al.,  
334 2007).

335  $^{40}\text{Ar}/^{39}\text{Ar}$  ages obtained on the same muscovite range from  $318.4 \pm 1.4$  Ma to  $309.7 \pm$   
336  $2.3$  Ma, in agreement with Late Carboniferous  $^{40}\text{Ar}/^{39}\text{Ar}$  ages ( $\sim 325$  to  $305$  Ma) of  
337 kinematically equivalent mylonitic rocks from the same and/or surrounding areas  
338 interpreted to reflect recrystallization ages from synmagmatic muscovite during  
339 leucogranite cooling (e.g. Gébelin et al., 2007, 2009). Based on the rapid cooling that  
340 followed the Millevaches granite syntectonic emplacement at  $313 \pm 4$  Ma within the  
341 dextral strike-slip Pradines shear zones (Gébelin et al., 2009) and protracted extensional  
342 shearing observed in the Felletin area at the roof of Millevaches leucogranites through  
343 the brittle-ductile transition (Fig. 3A), ages of  $316.7 \pm 0.7$  Ma (MIL 19,  $\delta D_{Ms} = -109‰$ ),

344 314.0 ± 0.6 Ma (MIL 18D,  $\delta D_{Ms} = -105\text{‰}$ ) and 313.6 ± 0.6 Ma (MIL 18C,  $\delta D_{Ms} = -104\text{‰}$ )  
345 are interpreted to reflect the timing of detachment activity during meteoric fluid infiltration.  
346 This interpretation is strengthened by microstructural observations supporting mica fish  
347 recrystallization by solution-precipitation processes (Fig. 3B), and by the chemical  
348 zonation of muscovite fish indicating high Mg and Fe, and low Na contents in their rims  
349 in contrast to their cores (EPMA data; Fig. SM1; Table SM2). This core-rim contrast has  
350 been correlated with deuterium depletion of syntectonic muscovite fish and often  
351 interpreted to reflect hydrothermal alteration in syntectonic leucogranite (e.g. Miller et al.,  
352 1981, G ebelin et al., 2011). Also, euhedral and unzoned muscovite from undeformed  
353 samples (see EPMA data of sample MIL18I) present similar chemical compositions than  
354 those observed in the cores of depleted micafish, reinforcing the interpretation that  
355 meteoric fluid interaction impacted muscovite chemistry. Therefore, we interpret  
356 muscovite fish zonation in deformed samples as resulting from muscovite syntectonic  
357 recrystallisation by dissolution-precipitation in presence of meteoric fluids.

358 Ages of 318.4 ± 1.4 Ma and 309.7 ± 2.3 Ma suggested by the saddle shaped age  
359 spectrum yielded by muscovite from the syntectonic pegmatite (MIL 18H,  $\delta D_{Ms} = -116\text{‰}$ )  
360 indicate partial recrystallization as late as ~310 Ma (e.g. Alexandrov et al., 2002) and  
361 may represent the upper and lower bounds of extensional ductile shearing, respectively.

362 Muscovite from the undeformed leucogranite sample MIL18I collected at the bottom of  
363 the detachment section (Fig. 3) yields an  $^{40}\text{Ar}/^{39}\text{Ar}$  age of 314.6 ± 0.7 Ma. The same  
364 muscovite provided higher  $\delta D_{Ms}$  values of -96‰ that, compared to lower values obtained  
365 on sheared leucogranite samples suggesting a meteoric fluid-rock exchange during  
366 deformation-induced recrystallization, could indicate a lower meteoric fluid/rock ratio  
367 and/or a magmatic fluid signature. In agreement with its structural level (90 m from  
368 sample MIL19), euhedral shape, and magmatic composition (low-Mg, low-Fe, high-Na),  
369 this undeformed muscovite sample remained unaffected by extensional deformation and  
370 likely had no interaction with meteoric fluids. Therefore, we consider that the undeformed  
371 muscovite from the MIL18I sample recorded cooling below the isotopic closure  
372 temperature of muscovite (~400 ± 50°C) at ~315 Ma.

373 Interestingly, muscovite that recrystallized on a fault plane (MIL13A) in the upper crust  
374 provides an  $^{40}\text{Ar}/^{39}\text{Ar}$  age of  $313.8 \pm 0.7$  Ma which is comparable to those obtained on  
375 mica fish from syntectonic granite emplaced in the Felletin detachment footwall. This  
376 muscovite  $^{40}\text{Ar}/^{39}\text{Ar}$  plateau age corresponds with relative chronology indicating a start  
377 for movement along the N020-striking Felletin-Ambrugeat Fault System at  $\sim 315$  Ma (e.g.  
378 Cartannaz et al., 2007), demonstrating coeval extension in both the upper and lower  
379 crust at  $\sim 315$  Ma. In addition, U/Pb data indicate that syntectonic leucogranite  
380 emplacement along the Pradines dextral strike-slip shear zone and migmatization of the  
381 lower crust also occurred at  $\sim 315$  Ma in the center of the Millevaches massif (Gébelin et  
382 al., 2009). As suggested for the western part of the French Massif Central (e.g. Burg et  
383 al., 1994; Gébelin et al., 2009), these geochronological results reinforce the idea that late  
384 Variscan tectonics were characterized by coeval transpression and extension.  
385 Importantly, the consistency of U/Pb and  $^{40}\text{Ar}/^{39}\text{Ar}$  ages amongst several rock types at  
386 varying crustal depths indicates that Earth's surface fluids reached significant depth in  
387 the Millevaches massif during the Late Carboniferous, as facilitated by synconvergent  
388 stretching of the upper crust and coeval high heat flux (which is consistent with previous  
389 studies; e.g. Person et al., 2007; Gébelin et al., 2017).

390 From the samples we have studied in this section, we propose that low  $\delta\text{D}_{\text{Ms}}$  values from  
391 the Millevaches massif were likely acquired between  $318.4 \pm 1.4$  Ma and  $309.7 \pm 2.3$  Ma  
392 during coeval high-temperature deformation and meteoric fluid-rock interactions; the age  
393 span reflecting the syntectonic growth of mica through time during the shear zone activity  
394 (e.g. Gébelin et al., 2011). Calculated  $\delta\text{D}_{\text{water}}$  values as low as  $-104\text{‰}$  can be interpreted  
395 to reflect a maximum value for meteoric water as the  $\delta\text{D}_{\text{water}}$  values at the surface may  
396 have been potentially lower due to water-rock isotope exchange at depth that inevitably  
397 shift the isotope composition of water to more positive values. However, we consider the  
398 average of the lowest 30% of the data ( $\delta\text{D}_{\text{water}}$  value =  $-96 \pm 8\text{‰}$ ;  $n=3$ ) to represent a  
399 conservative estimate for the hydrogen isotopic composition of surface-derived fluids  
400 that exchanged with hydrous minerals at depth during high temperature deformation at  
401  $\sim 315$  Ma.

#### 402 **4.2. Reconstruction of meteoric water composition in the foreland**

403 By comparison with modern and Jurassic euryhaline sharks (e.g. Dera et al., 2009), we  
404 used a phosphate-water isotope exchange temperature of  $29 \pm 3^\circ\text{C}$  (e.g. Fischer et al.,  
405 2013) to calculate the oxygen isotopic composition of the fresh water in which the ~295  
406 Ma-old sharks evolved. Therefore, using the  $\delta^{18}\text{O}_\text{P}$  values obtained from lifelong and  
407 short-lived shark proxies (Fisher et al. 2013), and the phosphate-water oxygen  
408 fractionation equation (Lécuyer et al., 2013) at a temperature of  $29 \pm 3^\circ\text{C}$ , we calculate  
409  $\delta^{18}\text{O}_\text{water}$  values of  $-4.1\text{‰}$  to  $-2.1\text{‰} \pm 0.7\text{‰}$  ( $n=17$ ). We interpret these values to represent  
410 the oxygen isotopic composition of fresh water in low-altitude basins during the Late  
411 Carboniferous (Table 2). For the paleoaltimetry reconstruction, an average of the lowest  
412 30% of the  $\delta^{18}\text{O}_\text{water}$  values of  $-3.8 \pm 0.8\text{‰}$  (see Table 2 and Figs. 4B and 4C for details  
413 and uncertainties) is used to account for potential evaporative enrichment in  $^{18}\text{O}$ . This  
414 value is consistent with a near-coastal position and low-elevation meteoric water.

#### 415 **4.3. How high was the Limousin region during the Late Carboniferous?**

416 Given the broad range of uncertainties surrounding Carboniferous climate impacts on  
417 hydrogen and oxygen isotopes in precipitation, we rely on a comparison of  $\delta\text{D}_\text{water}$  (or  
418  $\delta^{18}\text{O}_\text{water}$ ) at high and low elevation, thus, reducing uncertainties of our paleoaltimetry  
419 estimates largely to the uncertainties of the isotopic lapse rate. We, therefore, compare  
420  $\delta\text{D}$  values of meteoric water retrieved from ~315 Ma mylonitic rocks in the hinterland  
421 ( $\delta\text{D}_\text{water} = -96 \pm 8\text{‰}$  or  $\delta^{18}\text{O}_\text{water} = -13.3 \pm 1.1\text{‰}$ ) with  $\delta^{18}\text{O}_\text{water}$  values calculated from ~295  
422 Ma freshwater shark remains preserved in the Bourbon l'Archambault foreland basin  
423 ( $\delta\text{D}_\text{water} = -20 \pm 6\text{‰}$  or  $\delta^{18}\text{O}_\text{water} = -3.8 \pm 0.8\text{‰}$ ; Figs. 4 and 5).

424 The difference in  $\delta\text{D}_\text{water}$  values of Late Carboniferous meteoric water between the  
425 Felletin detachment mylonites in the hinterland and the Bourbon l'Archambault foreland  
426 basin is  $\Delta\delta\text{D}_\text{water} = 76 \pm 15\text{‰}$  (or  $\Delta\delta^{18}\text{O}_\text{water} = 9.5 \pm 1.9\text{‰}$ ). Using a lapse rate of  $-22\text{‰}/\text{km}$   
427 for  $\delta\text{D}_\text{water}$  values (e.g. Poage and Chamberlain, 2001), this difference in isotopic  
428 compositions indicates an elevation difference of  $3.4 \pm 0.7$  km (Figs. 4 and 5). However,  
429 if we use a present-day tropical lapse rate of  $-14.6\text{‰}/\text{km}$  (Saylor et al., 2009), we obtain  
430 a higher calculated elevation difference of  $5.2 \pm 1.1$  km (Table SM7B). Since we cannot

431 rule out that the time interval of interest in this study was characterized by globally cooler  
432 temperatures, 1D-Rayleigh fractionation model lapse rates for mean annual  
433 temperatures 5°C lower than today would result in calculated paleoelevation of  $3.2 \pm 0.5$   
434 km (Fig. SM3; see e.g. Jackson et al., 2019).

435 The error estimate on elevation quantification includes the isotope analyses ( $\delta D_{Ms} \pm 2\text{‰}$ ;  
436  $\delta^{18}O_P \pm 0.2\text{‰}$ ), the average of the lowest 30% of the isotope ratios ( $\delta D_{Ms} \pm 6\text{‰}$ ;  $\delta^{18}O_P \pm$   
437  $0.3\text{‰}$ ) and the temperature estimates (muscovite  $\pm 51^\circ\text{C}$ ; sharks  $\pm 3^\circ\text{C}$ ), but excludes  
438 any uncertainty on the isotope lapse rate, which under present-day conditions attains ca.  
439  $\pm 0.7$  km for model elevations of  $\sim 3.4$  km (Rowley, 2007).

440 We hence consider paleoelevations in excess of  $\sim 3$  km to represent the preferred  
441 estimate for mean paleoelevation of the French Massif Central at  $\sim 315$  Ma. It is clear  
442 that changes in atmospheric stratification, air mass blocking, evapotranspiration, relative  
443 humidity and air parcel trajectories are largely unconstrained but affected isotope lapse  
444 rates in the Carboniferous. However, by exploring a range of feasible lapse rates, we  
445 feel confident to reliably provide stable isotope elevation constraints for a segment of  
446 one of the largest orogens in Phanerozoic history.

#### 447 **4.4. Assumptions/limitations of paleoaltimetry calculations**

448 Paleoelevation estimates of ca. 3.2 - 5.2 km calculated using the isotopic composition of  
449 ancient rainwater recorded in the hinterland and foreland areas serve as first  
450 approximations due to the  $\sim 20$  Ma age difference between the two proxies ( $\sim 315$  Ma for  
451 mylonites and  $\sim 295$ - $290$  Ma for sharks).

452 We consider elevations in excess of  $\sim 3$  km as robust for the following reasons: First, the  
453 average  $\delta D_{\text{water}}$  value of  $-96 \pm 8\text{‰}$  retrieved from the Felletin detachment footwall  
454 represents a maximum value as any  $\delta D_{\text{meteoric water}}$  value at the Earth's surface would likely  
455 be more negative (e.g. Gébelin et al., 2012). Second, using the lowest  $\delta D_{Ms}$  value of -  
456  $116\text{‰}$  obtained from a syntectonic pegmatite (MIL18H), we calculate a  $\delta D_{\text{water}}$  value of -  
457  $104\text{‰}$  (Table 1) that, reflecting a larger time-integrated meteoric fluid/rock ratio, most  
458 closely approximates the isotopic composition of meteoric water at the Earth's surface.  
459 Referencing this lowest  $\delta D_{\text{water}}$  value to our near sea level record would increase  $\Delta\delta D$  to

460 84‰ and using the lapse rate of Poage and Chamberlain (2001) our paleoelevation  
461 estimate to  $\Delta z = 3.8 \pm 0.7$  km (Table SM7C). At the same time, the structural position of  
462 the sample with the lowest  $\delta D_{Ms}$  value (-116‰; MIL18H) does not follow a simple linear  
463 trend of increasing  $\delta D_{Ms}$  values with increasing distance to the detachment (Fig. 3C)  
464 suggesting that fluid flow occurred in a localized fashion as has been observed in similar  
465 studies (e.g. G ebel et al., 2011). If we were to exclude this value, our paleoelevation  
466 estimates based on the average of the other datapoints would decrease to  $3.0 \pm 0.7$  km  
467 as  $\Delta \delta D$  decreases to 67‰ (Table SM7D). Third, the Bourbon l'Archambault foreland  
468 basin is situated ~100 km from the hinterland sites on the downwind side in the current  
469 geographic configuration (Fig. 1). However, the average  $\delta^{18}O_{water}$  value of  $-3.8 \pm 0.9$ ‰  
470 obtained from the Bourbon l'Archambault basin is relatively low compared to those  
471 calculated from shark remains on the windward side from the Guardia Pisano basin in  
472 Italy ( $-2.1 \pm 0.9$ ‰; n=23; Fig. SM2; Table SM5; Fischer et al., 2013) that would lead to  
473 higher paleoelevation estimates of  $4.0 \pm 0.7$  km (Table SM7E). Fourth, an increase of  
474 1.5‰ in  $\delta^{18}O_{ocean\ water}$  values (+12‰ in  $\delta D$ ) is expected due to storage of low  $\delta^{18}O$  ice in  
475 the Antarctic ice shield or in continental glaciers (Buggisch et al., 2008).

#### 476 **4.5. Paleoclimatic implications of a moderate-elevation Variscan belt**

477 The Late Paleozoic Ice Age was characterized by voluminous ice sheets in southern  
478 Gondwana (e.g. Gonz alez-Bonorino and Eyles, 1995) and rapid fluctuations between  
479 glacial and interglacial conditions (e.g. Michel et al., 2015; Scheffler et al., 2003), with a  
480 major glaciation at ~315 Ma (e.g. Monta nez and Poulsen, 2013) and peak icehouse  
481 conditions at ~298-295 Ma (Soreghan et al., 2019), followed by an increasingly arid  
482 Permian climate (e.g. Tabor and Poulsen, 2008). During the Late Carboniferous, the  
483 Pangea assemblage moved northward from 10 S to ~5 N between ~315 and ~290 Ma  
484 (e.g. Edel et al., 2018; Kent and Muttoni, 2020) and was characterized by a unique and  
485 long E-W trending mountain chain, including the French Massif Central (Fig. 1, e.g.  
486 Domeier and Torsvik, 2014). This large Paleozoic belt most likely represented an  
487 orographic barrier that impacted the transport of air masses mainly coming from the  
488 Paleotethys Ocean located to the southeast (Fig. 1; e.g. Fluteau et al., 2001; Tabor and

489 Poulsen, 2008). A comparison with modern conditions suggests that the Variscan  
490 mountain range was favorable to high precipitation rates on its southern flank and  
491 insulating warm and moist tropical air over the southern Gondwana region from the drier  
492 and colder air masses to the north in Laurussia (e.g. Fluteau et al., 2001). Although  
493 Laurussia may have been characterized by an orographic rain shadow (e.g. Fluteau et  
494 al., 2001), there is evidence for progressive aridification of Laurussia linked to the closure  
495 of the Rheic ocean and not to the presence of a mountain chain blocking air masses  
496 from the south (e.g. Roscher and Schneider, 2006). However, global atmospheric  
497 circulation models simulating paleoclimate of Andean surface uplift indicate that only  
498 50% of the modern Andean plateau topography (~2000 m) is sufficient to deflect  
499 prevalent air masses from the Pacific ocean, and trigger a South American Low Level  
500 Jet where moisture comes from the Equatorial Atlantic (e.g. Insel et al., 2010). Moreover,  
501 a rain shadow effect from the Appalachian orogen has been evidenced based on H  
502 isotopic analysis of 318-308 Ma clays in the Appalachian Plateau with  $\delta D_{\text{water}}$  values  
503 down to -72‰ (Boles and van der Pluijm, 2020). Therefore, we propose that even at  
504 restrained mean altitude, the Carboniferous Variscan belt of western Europe would have  
505 influenced continental moisture transport and associated air mass trajectories.

#### 506 **4.6. How does a medium Variscan mean elevation fit with the Late Carboniferous** 507 **geological record?**

508 A mean elevation exceeding ~3 km is in good agreement with the interpretation of the  
509 French Massif Central as a segment of thickened crust resulting from the tectonic  
510 accretion of Armorica and Gondwana and the closure of the Medio-European ocean (e.g.  
511 Matte, 2001). Our results are also consistent with rapid erosion whose products are  
512 found in the French Massif Central such as Namurian olistoliths (330-325 Ma),  
513 Westphalian turbidites and coarse conglomerates (325-304 Ma) and Stephanian  
514 deposits (304-299 Ma) (e.g. Franke and Engel, 1986; Pfeifer et al., 2018). Stephanian  
515 basins are usually concentrated in narrow and elongated zones that could be interpreted  
516 to reflect the bottom of ancient restricted valleys, reinforcing the presence of an active  
517 mountain chain. However, Late Carboniferous-Early Permian coal deposits do not

518 support a very high elevation plateau (e.g. Kent and Muttoni, 2020; Strullu-Derrien et al.,  
519 2021). Although the Westphalian and Stephanian deposits support the presence of a  
520 topographic high, the activity of detachment zones during the Late Carboniferous  
521 indicates that the orogen was collapsing (e.g. Burg et al., 1994; Vanderhaeghe et al.,  
522 2020, and references therein).

#### 523 **4.7. Tectonic implications**

524 Although the Variscan belt displays undeniable similarities with the Tibet-Himalaya  
525 orogen in its tectonic style and geochemistry of partially molten rocks exhumed in the  
526 footwall of detachment faults (e.g. Dörr and Zulauf, 2010), our paleoaltimetry estimates  
527 indicate that at ~315 Ma the French Massif Central region was high but not necessarily  
528 similar in its topography to the present-day Himalayan ranges.

529 Possible explanations include the rheology of the material involved during the  
530 mechanisms of deformation during the Paleozoic. Based on the large amount of partially  
531 molten rocks, the radioactive heat production of the overthickened crust and the high  
532 geothermal gradient, the Variscan belt of western Europe is considered a “hot orogen”  
533 where the low viscosity material allows the crust to flow from the hinterland to the foreland  
534 (e.g. Vanderhaeghe et al., 2020, and references therein). It is therefore possible that a  
535 rather soft and hot crust together with the activity of detachment zones characterizing  
536 the Variscan orogen at the end of the orogenic cycle did not support soaring heights,  
537 even in the core of the Variscan belt, prior to synorogenic extension. Therefore, our  
538 paleoaltimetry estimate exceeding ~3 km is consistent with the thermal state that  
539 characterized this part of the orogen during the Late Carboniferous (e.g. Franke, 2014;  
540 Vanderhaeghe et al., 2020). However, our results suggest that the Central Pangea  
541 mountain belt was high enough to block air masses from the south-south-east and induce  
542 an orographic rainshadow to the north, playing a major role on the Earth’s climate at the  
543 end of the Carboniferous.

544 **5. Conclusion**

545 Comparison of Late Carboniferous stable isotope multi-proxy records from sites in the  
546 internal zone of the Variscan belt (Felletin, French Massif Central) and near sea level  
547 (Bourbon l'Archambault basin) allows to quantify the paleoelevation of a major Paleozoic  
548 orogen. The low  $\delta D$  values of meteoric water retrieved from ~315 Ma-old synkinematic  
549 hydrous minerals in the Felletin detachment footwall (Millevaches massif) reflect  
550 precipitation captured at high ( $> \sim 3$  km) elevation during the Late Carboniferous. When  
551 compared to age-equivalent near-sea level records obtained from freshwater shark  
552 remains, differences in  $\delta^{18}O_{\text{water}}$  and  $\delta D_{\text{water}}$  compositions are consistent with minimum  
553 elevations of  $\sim 3.4 \pm 0.7$  km. These results agree with geodynamic models emphasizing  
554 the role of partially molten rocks and magmatism in Variscan crustal evolution, reinforcing  
555 its characteristic feature of "hot collisional orogen". However, though the Variscan belt of  
556 Western Europe cannot be compared from a topographic point of view to the highest  
557 modern Himalayan mountains, our paleoaltimetry estimates imply that this orogen  
558 represented a major barrier, very likely blocking air masses from the Paleotethys and  
559 generating an orographic rain shadow to the north at the end of the Carboniferous.

560 **6. Acknowledgements**

561 CD acknowledges a PhD studentship from the University of Plymouth (UK). The authors  
562 are grateful to J. Fiebig and U. Treffert for laboratory support and to P. Boulvais and S.  
563 Grimes for fruitful discussions. The authors acknowledge the thoughtful and constructive  
564 reviews by Lily S. Pfeifer and Joel E. Saylor that greatly improved the manuscript.

565 **7. References**

566 Alexandrov, P., Ruffet, G., Cheilletz, A., 2002. Muscovite recrystallization and saddle-  
567 shaped  $40 \text{ Ar}/39 \text{ Ar}$  age spectra: example from the Blond granite (Massif Central,  
568 France). *Geochim. Cosmochim. Acta* 66, 1793–1807.  
569 [https://doi.org/10.1016/S0016-7037\(01\)00895-X](https://doi.org/10.1016/S0016-7037(01)00895-X)

570 Becq-Giraudon, J.-F., Montenat, C., Van Den Driessche, J., 1996. Hercynian high-altitude  
571 phenomena in the French Massif Central: tectonic implications. *Palaeogeogr.*  
572 *Palaeoclimatol. Palaeoecol.* 122, 227–241. [https://doi.org/10.1016/0031-](https://doi.org/10.1016/0031-0182(95)00081-X)  
573 [0182\(95\)00081-X](https://doi.org/10.1016/0031-0182(95)00081-X)

574 Boles, A., van der Pluijm, B., 2020. Locally Derived, Meteoric Fluid Infiltration Was  
575 Responsible for Widespread Late Paleozoic Illite Authigenesis in the Appalachian  
576 Basin. *Tectonics* 39, 0–3. <https://doi.org/10.1029/2020TC006137>

577 Boos, W.R., Kuang, Z., 2010. Dominant control of the South Asian monsoon by  
578 orographic insulation versus plateau heating. *Nature* 463, 218–222.  
579 <https://doi.org/10.1038/nature08707>

580 Buggisch, W., Joachimski, M.M., Sevastopulo, G., Morrow, J.R., 2008. Mississippian  
581  $\delta^{13}\text{C}_{\text{carb}}$  and conodont apatite  $\delta^{18}\text{O}$  records — Their relation to the Late  
582 Palaeozoic Glaciation. *Palaeogeogr. Palaeoclimatol. Palaeoecol.* 268, 273–292.  
583 <https://doi.org/10.1016/j.palaeo.2008.03.043>

584 Burg, J.P., Van Den Driessche, J., Brun, J.P., 1994. Syn- to post-thickening extension:  
585 mode and consequences. *Comptes Rendus - Acad. des Sci. Ser. II Sci. la Terre des*  
586 *Planetes* 319, 1019–1032.

587 Cartannaz, C., Rolin, P., Cocherie, A., Marquer, D., Legendre, O., Fanning, C.M., Rossi, P.,  
588 2007. Characterization of wrench tectonics from dating of syn- to post-magmatism  
589 in the north-western French Massif Central. *Int. J. Earth Sci.* 96, 271–287.  
590 <https://doi.org/10.1007/s00531-006-0101-y>

591 Dera, G., Pucéat, E., Pellenard, P., Neige, P., Delsate, D., Joachimski, M.M., Reisberg, L.,  
592 Martinez, M., 2009. Water mass exchange and variations in seawater temperature

593 in the NW Tethys during the Early Jurassic: Evidence from neodymium and oxygen  
594 isotopes of fish teeth and belemnites. *Earth Planet. Sci. Lett.* 286, 198–207.  
595 <https://doi.org/10.1016/J.EPSL.2009.06.027>

596 Domeier, M., Torsvik, T.H., 2014. Plate tectonics in the late Paleozoic. *Geosci. Front.* 5,  
597 303–350. <https://doi.org/10.1016/j.gsf.2014.01.002>

598 Dörr, W., Zulauf, G., 2010. Elevator tectonics and orogenic collapse of a Tibetan-style  
599 plateau in the European Variscides: the role of the Bohemian shear zone. *Int. J.*  
600 *Earth Sci.* 99, 299–325. <https://doi.org/10.1007/s00531-008-0389-x>

601 Dusséaux, C., Gébelin, A., Boulvais, P., Gardien, V., Grimes, S., Mulch, A., 2019. Meteoric  
602 fluid-rock interaction in Variscan shear zones. *Terra Nov.* 31, ter.12392.  
603 <https://doi.org/10.1111/ter.12392>

604 Edel, J.B., Schulmann, K., Lexa, O., Lardeaux, J.M., 2018. Late Palaeozoic palaeomagnetic  
605 and tectonic constraints for amalgamation of Pangea supercontinent in the  
606 European Variscan belt. *Earth-Science Rev.* 177, 589–612.  
607 <https://doi.org/10.1016/j.earscirev.2017.12.007>

608 Feulner, G., 2017. Formation of most of our coal brought Earth close to global glaciation.  
609 *Proc. Natl. Acad. Sci.* 114, 11333–11337.  
610 <https://doi.org/10.1073/pnas.1712062114>

611 Field, C.W., Fifarek, R.H., 1985. Light stable-isotope systematics in the epithermal  
612 environment, in: Berger, B.R., Bethke, P.M. (Eds.), *Geology and Geochemistry of*  
613 *Epithermal Systems*. Soc. of Econ. Geol., Boulder, Colorado, Colorado, pp. 99–128.  
614 <https://doi.org/10.5382/Rev.02.06>

615 Fischer, J., Schneider, J.W., Voigt, S., Joachimski, M.M., Tichomirowa, M., Tütken, T.,  
616 Götze, J., Berner, U., 2013. Oxygen and strontium isotopes from fossil shark teeth:  
617 Environmental and ecological implications for Late Palaeozoic European basins.  
618 Chem. Geol. 342, 44–62. <https://doi.org/10.1016/j.chemgeo.2013.01.022>

619 Fluteau, F., Besse, J., Broutin, J., Ramstein, G., 2001. The late Permian climate. What can  
620 be inferred from climate modelling concerning Pangea scenarios and Hercynian  
621 range altitude? Palaeogeogr. Palaeoclimatol. Palaeoecol. 167, 39–71.  
622 [https://doi.org/10.1016/S0031-0182\(00\)00230-3](https://doi.org/10.1016/S0031-0182(00)00230-3)

623 Franke, W., 2014. Topography of the Variscan orogen in Europe: Failed-not collapsed.  
624 Int. J. Earth Sci. 103, 1471–1499. <https://doi.org/10.1007/s00531-014-1014-9>

625 Franke, W., Engel, W., 1986. Synorogenic sedimentation in the Variscan Belt of Europe.  
626 Bull. la Société Géologique Fr. II, 25–33. <https://doi.org/10.2113/gssgfbull.II.1.25>

627 Gébelin, A., Brunel, M., Monié, P., Faure, M., Arnaud, N., 2007. Transpressional tectonics  
628 and Carboniferous magmatism in the Limousin, Massif Central, France: Structural  
629 and  $^{40}\text{Ar}/^{39}\text{Ar}$  investigations. Tectonics 26.  
630 <https://doi.org/10.1029/2005TC001822>

631 Gébelin, A., Jessup, M.J., Teyssier, C., Cosca, M.A., Law, R.D., Brunel, M., Mulch, A., 2017.  
632 Infiltration of meteoric water in the South Tibetan Detachment (Mount Everest,  
633 Himalaya): When and why? Tectonics 36, 690–713.  
634 <https://doi.org/10.1002/2016TC004399>

635 Gébelin, A., Martelet, G., Chen, Y., Brunel, M., Faure, M., 2006. Structure of late Variscan  
636 Millevaches leucogranite massif in the French Massif Central: AMS and gravity  
637 modelling results. J. Struct. Geol. 28, 148–169.

638 <https://doi.org/10.1016/j.jsg.2005.05.021>

639 Gébelin, A., Mulch, A., Teyssier, C., Heizler, M., Vennemann, T., Seaton, N.C.A., 2011.  
640 Oligo-Miocene extensional tectonics and fluid flow across the Northern Snake  
641 Range detachment system, Nevada. *Tectonics* 30, n/a-n/a.  
642 <https://doi.org/10.1029/2010TC002797>

643 Gébelin, A., Mulch, A., Teyssier, C., Jessup, M.J., Law, R.D., Brunel, M., 2013. The  
644 Miocene elevation of Mount Everest. *Geology* 41, 799–802.  
645 <https://doi.org/10.1130/G34331.1>

646 Gébelin, A., Mulch, A., Teyssier, C., Page Chamberlain, C., Heizler, M., 2012. Coupled  
647 basin-detachment systems as paleoaltimetry archives of the western North  
648 American Cordillera. *Earth Planet. Sci. Lett.* 335–336, 36–47.  
649 <https://doi.org/10.1016/j.epsl.2012.04.029>

650 Gébelin, A., Roger, F., Brunel, M., 2009. Syntectonic crustal melting and high-grade  
651 metamorphism in a transpressional regime, Variscan Massif Central, France.  
652 *Tectonophysics* 477, 229–243. <https://doi.org/10.1016/j.tecto.2009.03.022>

653 Gébelin, A., Teyssier, C., Heizler, M.T., Mulch, A., 2015. Meteoric water circulation in a  
654 rolling-hinge detachment system (northern Snake Range core complex, Nevada).  
655 *Bull. Geol. Soc. Am.* 127, 149–161. <https://doi.org/10.1130/B31063.1>

656 Goddéis, Y., Donnadiou, Y., Carretier, S., Aretz, M., Dera, G., Macouin, M., Regard, V.,  
657 2017. Onset and ending of the late Palaeozoic ice age triggered by tectonically  
658 paced rock weathering. *Nat. Geosci.* 10, 382–386.  
659 <https://doi.org/10.1038/ngeo2931>

660 González-Bonorino, G., Eyles, N., 1995. Inverse relation between ice extent and the late  
661 Paleozoic glacial record of Gondwana. *Geology* 23, 1015.  
662 [https://doi.org/10.1130/0091-7613\(1995\)023<1015:IRBIEA>2.3.CO;2](https://doi.org/10.1130/0091-7613(1995)023<1015:IRBIEA>2.3.CO;2)

663 Heavens, N.G., Mahowald, N.M., Soreghan, G.S., Soreghan, M.J., Shields, C.A., 2015. A  
664 model-based evaluation of tropical climate in Pangaea during the late Palaeozoic  
665 icehouse. *Palaeogeogr. Palaeoclimatol. Palaeoecol.* 425, 109–127.  
666 <https://doi.org/10.1016/j.palaeo.2015.02.024>

667 Insel, N., Poulsen, C.J., Ehlers, T.A., 2010. Influence of the Andes Mountains on South  
668 American moisture transport, convection, and precipitation. *Clim. Dyn.* 35, 1477–  
669 1492. <https://doi.org/10.1007/s00382-009-0637-1>

670 Jackson, L.J., Horton, B.K., Beate, B.O., Bright, J., Breecker, D.O., 2019. Testing stable  
671 isotope paleoaltimetry with Quaternary volcanic glasses from the Ecuadorian  
672 Andes. *Geology* 47, 1–4. <https://doi.org/10.1130/G45861.1>

673 Kent, D.V., Muttoni, G., 2020. Pangea B and the Late Paleozoic Ice Age. *Palaeogeogr.*  
674 *Palaeoclimatol. Palaeoecol.* 553, 109753.  
675 <https://doi.org/10.1016/j.palaeo.2020.109753>

676 Lécuyer, C., Amiot, R., Touzeau, A., Trotter, J., 2013. Calibration of the phosphate  $\delta^{18}\text{O}$   
677 thermometer with carbonate–water oxygen isotope fractionation equations.  
678 *Chem. Geol.* 347, 217–226. <https://doi.org/10.1016/j.chemgeo.2013.03.008>

679 Matte, P., 2001. The Variscan collage and orogeny (490-290 Ma) and the tectonic  
680 definition of the Armorica microplate: a review. *Terra Nov.* 13, 122–128.

681 Michel, L.A., Tabor, N.J., Montañez, I.P., Schmitz, M.D., Davydov, V.I., 2015.

682 Chronostratigraphy and Paleoclimatology of the Lodève Basin, France: Evidence for  
683 a pan-tropical aridification event across the Carboniferous–Permian boundary.  
684 *Palaeogeogr. Palaeoclimatol. Palaeoecol.* 430, 118–131.  
685 <https://doi.org/10.1016/j.palaeo.2015.03.020>

686 Miller, C.F., Stoddard, E.F., Bradfish, L.J., Dollase, W.A., 1981. Composition of plutonic  
687 muscovite; genetic implications. *Can. Mineral.* 19, 25–34.

688 Montañez, I.P., Poulsen, C.J., 2013. The Late Paleozoic Ice Age: An Evolving Paradigm.  
689 *Annu. Rev. Earth Planet. Sci.* 41, 629–656.  
690 <https://doi.org/10.1146/annurev.earth.031208.100118>

691 Mulch, A., 2016. Stable isotope paleoaltimetry and the evolution of landscapes and life.  
692 *Earth Planet. Sci. Lett.* 433, 180–191. <https://doi.org/10.1016/j.epsl.2015.10.034>

693 Mulch, A., Chamberlain, C.P., 2007. Stable Isotope Paleoaltimetry in Orogenic Belts The  
694 Silicate Record in Surface and Crustal Geological Archives. *Rev. Mineral.  
695 Geochemistry* 66, 89–118. <https://doi.org/10.2138/rmg.2007.66.4>

696 Mulch, A., Cosca, M.A., Andresen, A., Fiebig, J., 2005. Time scales of deformation and  
697 exhumation in extensional detachment systems determined by high-spatial  
698 resolution in situ UV-laser  $^{40}\text{Ar}/^{39}\text{Ar}$  dating. *Earth Planet. Sci. Lett.* 233, 375–390.  
699 <https://doi.org/10.1016/j.epsl.2005.01.042>

700 Mulch, A., Teyssier, C., Cosca, M.A., Vanderhaeghe, O., Vennemann, T.W., 2004.  
701 Reconstructing paleoelevation in eroded orogens. *Geology* 32, 525.  
702 <https://doi.org/10.1130/G20394.1>

703 Person, M., Mulch, A., Teyssier, C., Gao, Y., 2007. Isotope transport and exchange within

704 metamorphic core complexes. *Am. J. Sci.* 307, 555–589.  
705 <https://doi.org/10.2475/03.2007.01>

706 Pfeifer, L.S., Soreghan, G.S., Pochat, S., Van Den Driessche, J., Thomson, S.N., 2018.  
707 Permian exhumation of the Montagne Noire core complex recorded in the  
708 Graissessac-Lodève Basin, France. *Basin Res.* 30, 1–14.  
709 <https://doi.org/10.1111/bre.12197>

710 Poage, M.A., Chamberlain, C.P., 2001. Empirical relationships between elevation and the  
711 stable isotope composition of precipitation and surface waters: considerations for  
712 studies of paleoelevation change. *Am. J. Sci.* 301, 1–15.  
713 <https://doi.org/10.2475/ajs.301.1.1>

714 Poulsen, C.J., Pollard, D., Montañez, I.P., Rowley, D., 2007. Late Paleozoic tropical  
715 climate response to Gondwanan deglaciation. *Geology* 35, 771.  
716 <https://doi.org/10.1130/G23841A.1>

717 Roscher, M., Schneider, J.W., 2006. Permo-Carboniferous climate: Early Pennsylvanian  
718 to Late Permian climate development of central Europe in a regional and global  
719 context. *Geol. Soc. London, Spec. Publ.* 265, 95–136.  
720 <https://doi.org/10.1144/GSL.SP.2006.265.01.05>

721 Roscher, M., Schneider, J.W., 2005. An annotated correlation chart for continental Late  
722 Pennsylvanian and Permian basins and the marine scale. *The Nonmarine Permian.*  
723 *New Mex. Museum Nat. Hist. Sci. Bull.* 30, 282–291.

724 Rowley, D.B., 2007. Stable Isotope-Based Paleoaltimetry: Theory and Validation. *Rev.*  
725 *Mineral. Geochemistry* 66, 23–52. <https://doi.org/10.2138/rmg.2007.66.2>

- 726 Saylor, J.E., Mora, A., Horton, B.K., Nie, J., 2009. Controls on the isotopic composition of  
727 surface water and precipitation in the Northern Andes, Colombian Eastern  
728 Cordillera. *Geochim. Cosmochim. Acta* 73, 6999–7018.  
729 <https://doi.org/10.1016/j.gca.2009.08.030>
- 730 Scheffler, K., Hoernes, S., Schwark, L., 2003. Global changes during Carboniferous–  
731 Permian glaciation of Gondwana: Linking polar and equatorial climate evolution by  
732 geochemical proxies. *Geology* 31, 605. [https://doi.org/10.1130/0091-  
733 7613\(2003\)031<0605:GCDCGO>2.0.CO;2](https://doi.org/10.1130/0091-7613(2003)031<0605:GCDCGO>2.0.CO;2)
- 734 Soreghan, G.S., Soreghan, M.J., Heavens, N.G., 2019. Explosive volcanism as a key driver  
735 of the late Paleozoic ice age. *Geology* 47, 600–604.  
736 <https://doi.org/10.1130/G46349.1>
- 737 Stipp, M., Stünitz, H., Heilbronner, R., Schmid, S.M., 2002. The eastern Tonale fault zone:  
738 a ‘natural laboratory’ for crystal plastic deformation of quartz over a temperature  
739 range from 250 to 700°C. *J. Struct. Geol.* 24, 1861–1884.  
740 [https://doi.org/10.1016/S0191-8141\(02\)00035-4](https://doi.org/10.1016/S0191-8141(02)00035-4)
- 741 Strullu-Derrien, C., Cleal, C.J., Ducassou, C., Spencer, A.R.T., Stolle, E., Leshyk, V.O., 2021.  
742 A rare late Mississippian flora from Northwestern Europe (Maine-et-Loire Coalfield,  
743 Pays de la Loire, France). *Rev. Palaeobot. Palynol.* 285, 104359.  
744 <https://doi.org/10.1016/j.revpalbo.2020.104359>
- 745 Suzuoki, T., Epstein, S., 1976. Hydrogen isotope fractionation between OH-bearing  
746 minerals and water. *Geochim. Cosmochim. Acta* 40, 1229–1240.  
747 [https://doi.org/10.1016/0016-7037\(76\)90158-7](https://doi.org/10.1016/0016-7037(76)90158-7)
- 748 Tabor, N.J., Poulsen, C.J., 2008. Palaeoclimate across the Late Pennsylvanian–Early

749 Permian tropical palaeolatitudes: A review of climate indicators, their distribution,  
750 and relation to palaeophysiographic climate factors. *Palaeogeogr. Palaeoclimatol.*  
751 *Palaeoecol.* 268, 293–310. <https://doi.org/10.1016/j.palaeo.2008.03.052>

752 Taylor, H.P., 1977. Water/rock interactions and the origin of H<sub>2</sub>O in granitic batholiths.  
753 *J. Geol. Soc. London.* 133, 509–558. <https://doi.org/10.1144/gsjgs.133.6.0509>

754 Vanderhaeghe, O., Laurent, O., Gardien, V., Moyen, J.-F., Gébelin, A., Chelle-Michou, C.,  
755 Couzinié, S., Villaros, A., Bellanger, M., 2020. Flow of partially molten crust  
756 controlling construction, growth and collapse of the Variscan orogenic belt: the  
757 geologic record of the French Massif Central. *BSGF - Earth Sci. Bull.*  
758 <https://doi.org/10.1051/bsgf/2020013>

759 Wu, C.-M., Chen, H.-X., 2015. Calibration of a Ti-in-muscovite geothermometer for  
760 ilmenite- and Al<sub>2</sub>SiO<sub>5</sub>-bearing metapelites. *Lithos* 212–215, 122–127.  
761 <https://doi.org/10.1016/j.lithos.2014.11.008>

762

# Late Carboniferous paleoelevation of the Variscan Belt of Western Europe

Camille Dusséaux\*, Aude Gévelin, Gilles Ruffet, Andreas Mulch

\*Corresponding author: Camille Dusséaux ([ca.dusseaux@gmail.com](mailto:ca.dusseaux@gmail.com))

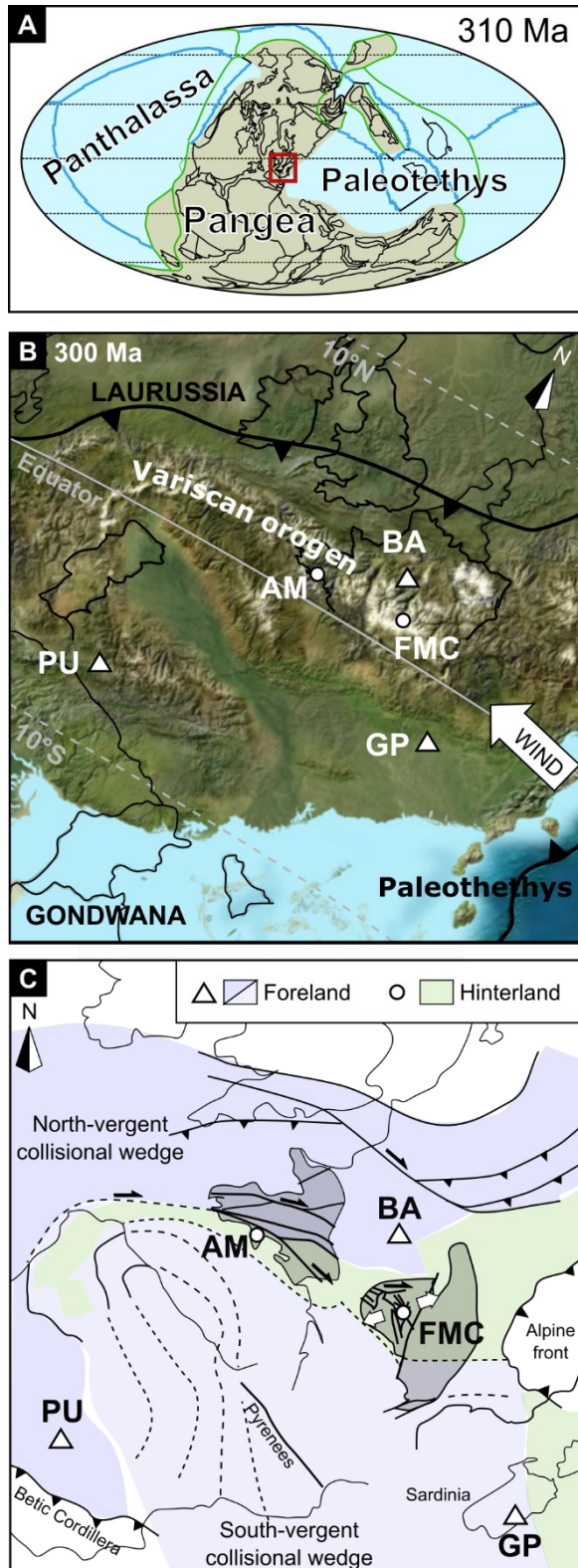


**Fig. 1.** (A) Late Carboniferous paleogeographic map (after Domeier and Torsvik, 2014). Red square indicates location of the study area in B. (B) Late Carboniferous paleogeographic map modified after Blakey (2011; downloaded in 2016; [www2.nau.edu/rcb7](http://www2.nau.edu/rcb7)). Modelled moisture transport direction is indicated by a white arrow (Tabor and Poulsen, 2008). (C) Simplified geological map of the Variscan belt of Western Europe modified after Franke et al. (2017) and Rubio Pascual et al. (2016). White circles and triangles indicate the location of our hinterland (syntectonic muscovite, this study) and foreland proxy records (freshwater shark teeth and spines; Fischer et al., 2013), respectively. AM: Armorican Massif, FMC: French Massif Central, PU: Puertollano basin, BA: Bourbon l'Archambault basin, and GP: Guardia Pisano basin.

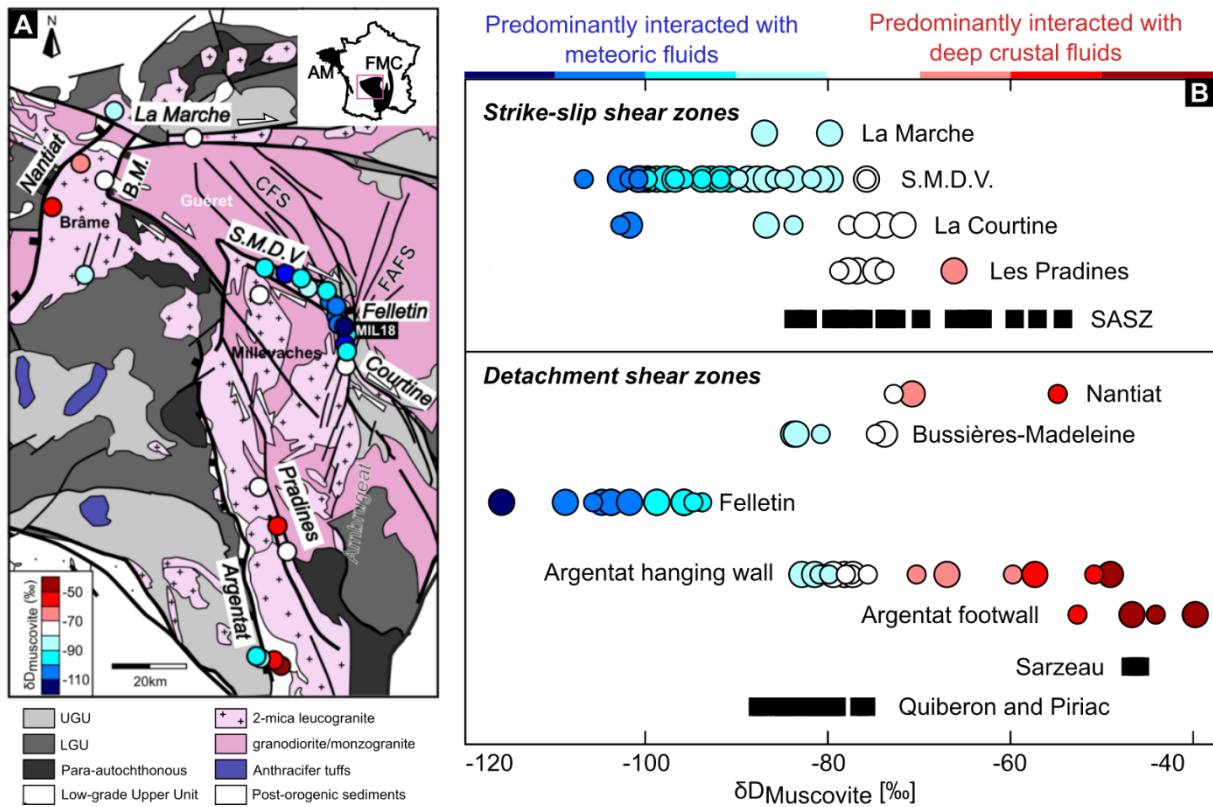


**Fig. 2.** (A) Geological map of the Limousin (western part of the French Massif Central) indicating sampling sites and results from hydrogen isotope ratios of synkinematic muscovite ( $\delta D_{\text{Ms}}$ ). (B)  $\delta D_{\text{Ms}}$  values obtained on syntectonic leucogranites, quartz veins and pegmatites from strike-slip and detachment shear zones in the Limousin (circles, this study) and Armorican Massif (black squares, Dusséaux et al., 2019). Small circle:  $250 < M_s \text{ fraction} < 500 \mu\text{m}$ ; large circle:  $M_s \text{ fraction} > 500 \mu\text{m}$ ; AM: Armorican Massif; FMC: French Massif Central; BM: Bussièrès-Madeleine; SMDV: Saint-Michel-de-Veisse; CFS: Creuse Fault System; FAFS: Felletin-Ambrugeat Fault System; SASZ: South Armorican Shear Zone (see text for interpretation).

Fig. 3.

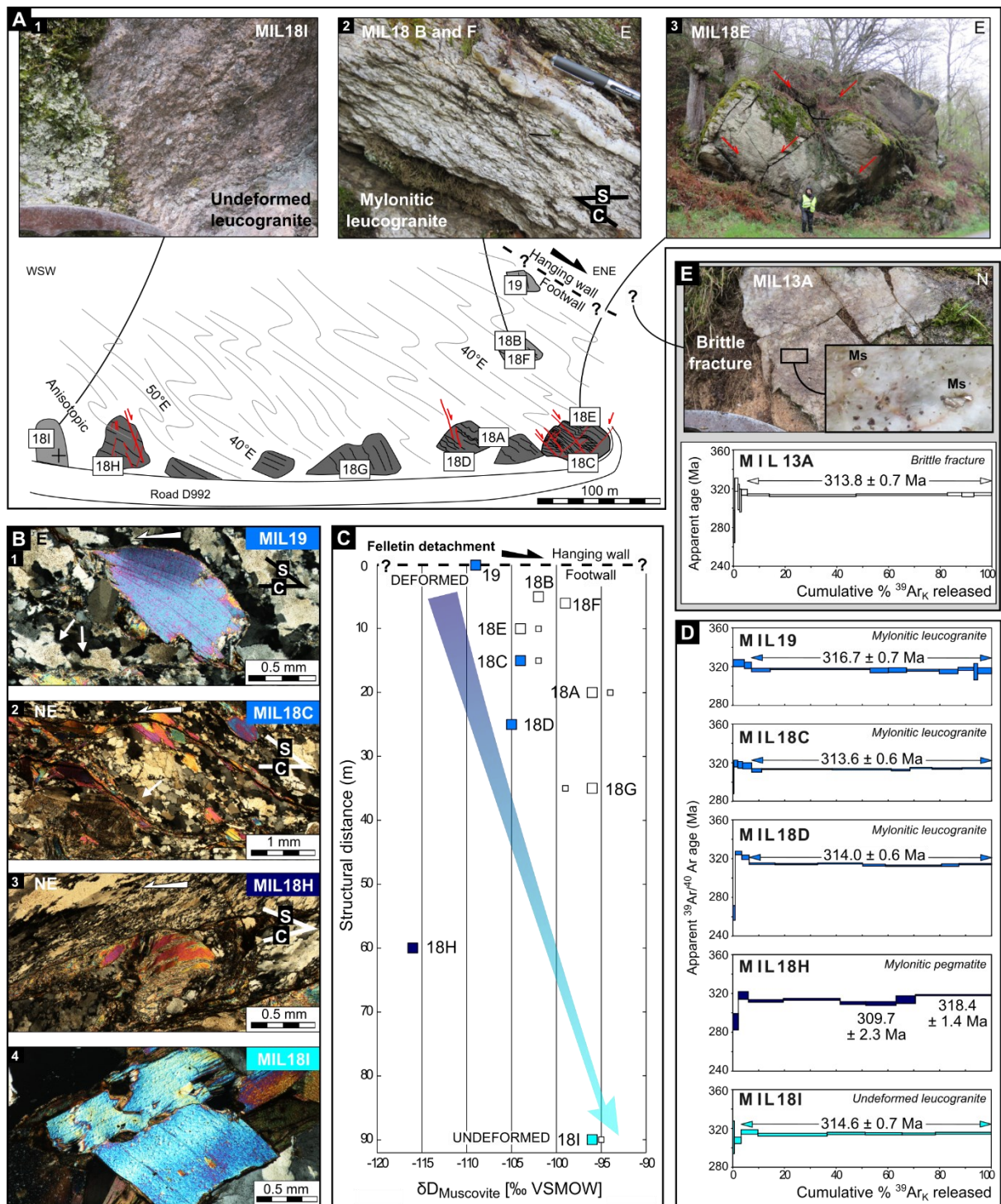
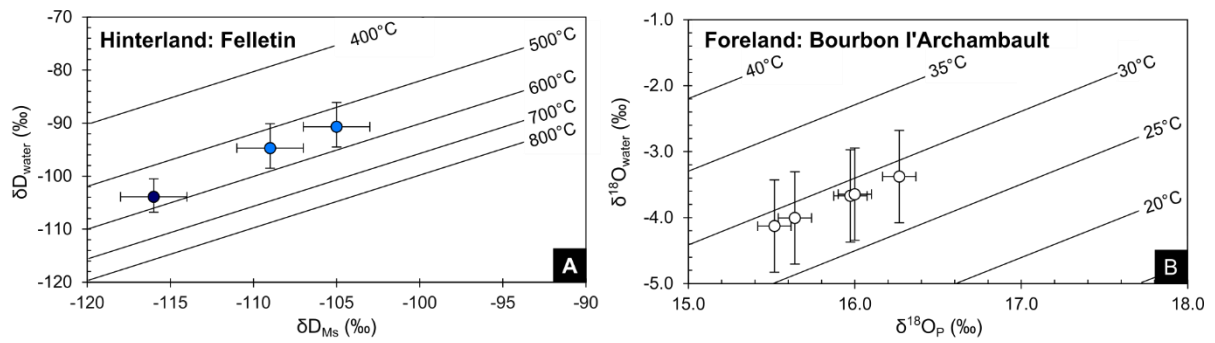


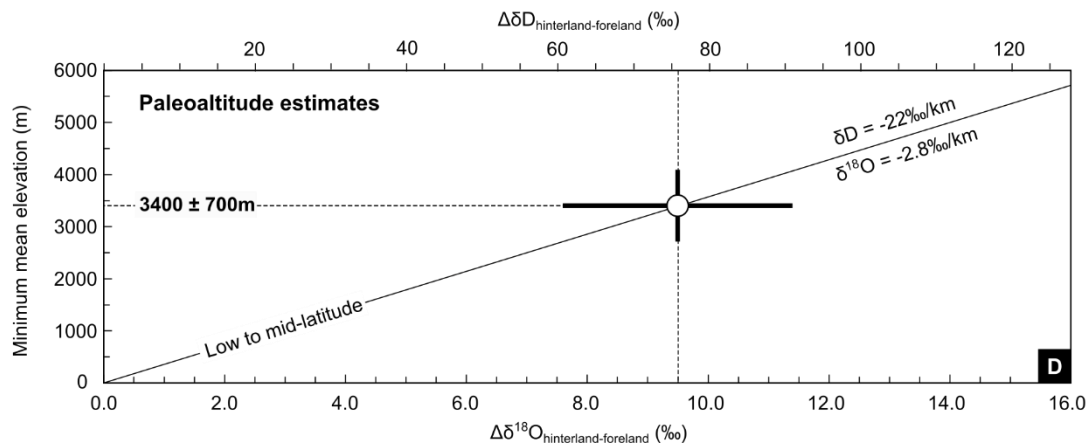
**Fig. 3.** (A) Felletin detachment footwall outcrop description (Millevaches massif, French Massif Central) showing location of studied samples. (B) Microstructure photographs of analyzed samples: (B1) Lenticular muscovite fish and quartz grains highlighting castellate boundaries (white arrows), (B2) Muscovite fish forming C-S structures and quartz showing grain-boundary migration, (B3) ultramylonitic facies displaying recrystallization of tiny muscovite grains within shear planes from primary muscovite and quartz recrystallization by subgrain rotation, (B4) euhedral muscovite grains in undeformed leucogranite. (C) Hydrogen isotope ratios of muscovite ( $\delta D_{Ms}$  values; small squares:  $250 < Ms \text{ fraction} < 500 \mu\text{m}$ ; large squares:  $Ms \text{ fraction} > 500 \mu\text{m}$ ) plotted against the estimated structural distance to the hanging wall (0 to 90 m). Note that point 18H does not follow a linear trend of increasing  $\delta D_{Ms}$  values with increasing distance to the detachment. (D)  $^{40}\text{Ar}/^{39}\text{Ar}$  step-heating spectra ( $1\sigma$ ) on single muscovite grains from leucogranite and pegmatite. (E)  $^{40}\text{Ar}/^{39}\text{Ar}$  step-heating spectra ( $1\sigma$ ) on single muscovite grains that crystallized on brittle fault plane and associated outcrop photograph. Samples analyzed in (D) are shown in blue colors in (B) and (C). See text for explanations.

**Fig. 4.** Uncertainties on the  $\delta D_{\text{water}}$  and  $\delta^{18}\text{O}_{\text{water}}$  values used for paleoaltimetry estimate calculations provided in (A) for the hinterland regions using the hydrogen isotope composition of synkinematic muscovite ( $\delta D_{Ms}$ ;  $n=3$ ), the temperatures of water-muscovite isotope exchange deduced from the titanium-in-muscovite geothermometer of Wu and Chen (2015) and the hydrogen isotope muscovite-water fractionation factor of Suzuoki and Epstein (1976), and in (B) for the foreland areas using the oxygen isotope composition of phosphate from shark teeth and spine ( $\delta^{18}\text{O}_P$ ;  $n=5$ ), a temperature of water-phosphate isotope exchange of  $29 \pm 3^\circ\text{C}$  deduced from modern and Jurassic euryhaline sharks (Dera et al., 2009; Fischer et al., 2013) and the hydrogen isotope phosphate-water fractionation factor of Lécuyer et al. (2013). (C) Table showing converted values from  $\delta D_{\text{water}}$  to  $\delta^{18}\text{O}_{\text{water}}$  values (and vice-versa) using the meteoric water line of Craig (1961). (D) Paleoaltitude estimates for the Variscan hinterland of Western Europe and associated uncertainties calculated for low and mid latitude (Poage and Chamberlain, 2001).

**Fig. 4.**



	Area	Proxy	Analysis	Values	$\pm$	$\pm$ (‰)	Average of	$\pm$	Average of	$\pm$
							$\delta D_{\text{Water}}$ values (‰)		$\delta^{18}\text{O}_{\text{Water}}$ values (‰)	
<b>Hinterland</b>	Felletin	Muscovite	Isotope analysis ( $\delta D_{\text{Ms}}$ values)	From -116‰ to -105‰	2‰	2‰	-96	8	-13.3	1.1
			Average of $\delta D_{\text{Ms}}$ values	-110‰	6‰	6‰				
			Temperature Ti-in-Ms	540°C	51°C	5‰				
<b>Foreland</b>	Bourbon l'Archambault	Shark remains	Isotope analysis ( $\delta^{18}\text{O}_P$ values)	From 15.5‰ to 16.3‰	0.2‰	0.2‰	-20	6	-3.8	0.8
			Average of $\delta^{18}\text{O}_P$ values	15.9‰	0.3‰	0.5‰				
			Water temperature	29°C	3°C	0.7‰				



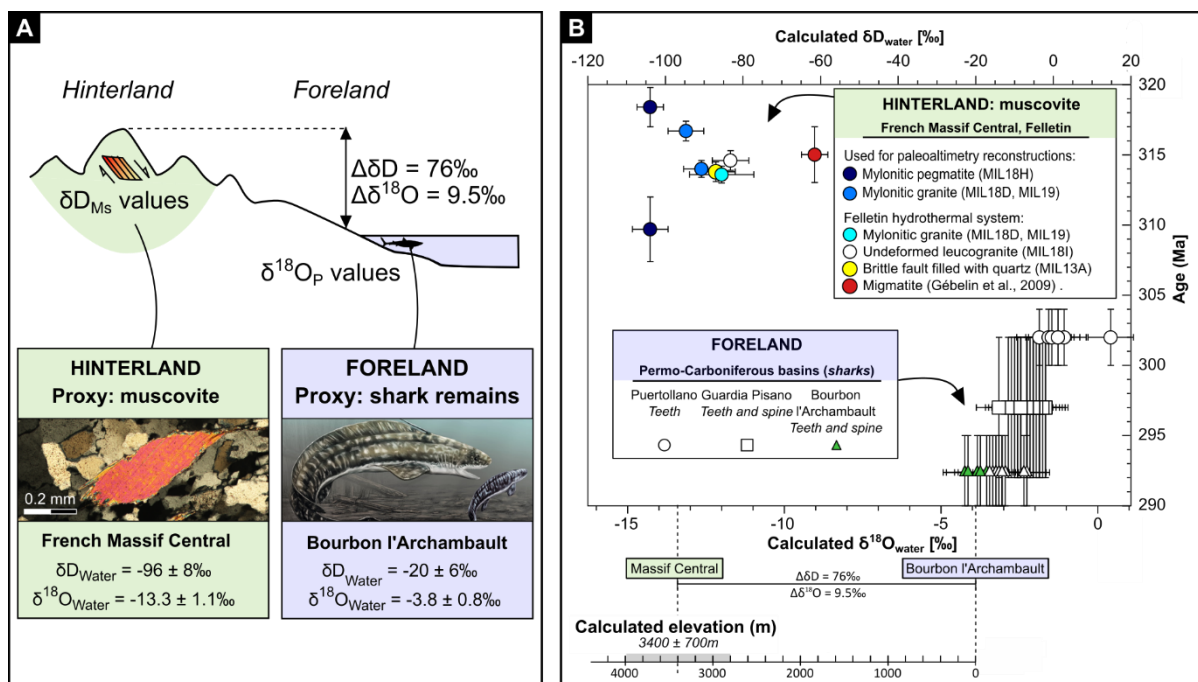


**Fig. 5.** (A) Schematic cross-section showing the location of proxies and data used for paleoaltimetry reconstructions. (B)  $\delta D_{water}$  values calculated from synkinematic muscovite from the hinterland versus their  $^{40}Ar/^{39}Ar$  ages, and  $\delta^{18}O_{water}$  values calculated from shark remains in the foreland versus their biostratigraphic and isotopic ages. Difference in  $\delta^{18}O_{water}$  values of  $\sim 9.5\text{‰}$  between hinterland proxies (Felletin) and foreland proxies (Bourbon l'Archambault foreland basin) is consistent with Late Carboniferous paleoelevation of the French Massif Central in excess of  $\sim 3.0$  km (see also Fig. 4). Hydrogen and oxygen isotopes, and geochronological data are detailed in Table SM6. Sharks drawing courtesy of Alain Bénétiau.

Sample	Distance (m)	Rock type	$\delta D_{Ms}$ (‰ VSMOW)	Uncertainty (‰)	Fraction Ms ( $\mu m$ )	T (°C)	Uncertainty (°C)	$\delta D_{water}$ (‰ VSMOW)	-	+
MIL19	0	Mylonitic leucogranite	-109	2	500<f	540	51	<b>-95</b>	-4	5
MIL18B	5	Mylonitic leucogranite	-102	2	500<f	540	51	<b>-88</b>	-4	5
MIL18F	6	Quartz vein	-99	2	500<f	540	51	<b>-85</b>	-4	5
MIL18E	10	Mylonitic leucogranite	-104	2	500<f	540	51	<b>-90</b>	-4	5
MIL18C	15	Mylonitic leucogranite	-104	2	500<f	<b>493</b>	<b>57</b>	<b>-86</b>	-5	8
MIL18A	20	Mylonitic leucogranite	-96	2	500<f	540	51	<b>-82</b>	-4	5
MIL18D	25	Mylonitic leucogranite	-105	2	500<f	540	51	<b>-91</b>	-4	5
MIL18G	35	Mylonitic leucogranite	-99	2	250<f<500	540	51	<b>-85</b>	-4	5
MIL18H	60	Mylonitic pegmatite	-116	2	500<f	<b>568</b>	<b>42</b>	<b>-104</b>	-3	3
MIL18I	90	Undeformed leucogranite	-96	2	500<f	<b>559</b>	<b>55</b>	<b>-83</b>	-4	5
<b>AVERAGE of MIL19, MIL18D and MIL18H</b>			<b>-110</b>					<b>-96</b>	-4	4
SD			6					<b>7</b>	1	1
Min			-116					<b>-104</b>	-3	3
Max			-105					<b>-91</b>	-4	5

**Table 1.**  $\delta D_{water}$  values and uncertainties calculated using the temperatures of muscovite-water hydrogen isotope exchange obtained from the Ti-in-Ms geothermometer (Wu and Chen, 2015), the measured  $\delta D_{Ms}$  values from syntectonic leucogranites emplaced in the Felletin detachment footwall (NE corner of the Millevaches massif) and the hydrogen isotope fractionation factor of Suzuoki and Epstein (1976). Grey lines indicate data used for paleoaltimetry reconstruction.

Locality	Formatio	Age	Taxon	Sample	Material	$\delta^{18}\text{O}_\text{P}$ (‰ VSMOW)	$^{87}\text{Sr}/^{86}\text{Sr}$	T (°C)	$\pm$ (°C)	$\delta^{18}\text{O}_\text{water}$ (‰ VSMOW)	$\pm$ (°C)			
Bourbon l'Archambault Basin (France)	Buxières Fm	Early Permian, Sakmarian (295 - 290 Ma)	<i>Lissodus</i>	LBS 1A	fin spine	16.7	0.71070	29	3	-2.9	0.7			
				LBS 1B	fin spine	16.9		29	3	-2.8	0.7			
				LBS 2	fin spine	16.4	0.71058	29	3	-3.2	0.7			
				LBS 2A	fin spine	16.6		29	3	-3.1	0.7			
				LBS 2B	fin spine	16.7		29	3	-2.9	0.7			
				LBS 2C	fin spine	16.7		29	3	-3.0	0.7			
				LBS 3	fin spine	15.6	0.71077	29	3	-4.0	0.7			
				LBS 3A	fin spine	16.0		29	3	-3.7	0.7			
				LBS 3B	fin spine	15.5		29	3	-4.1	0.7			
				<i>Orthacanthus buxieri</i>	OB1	tooth enameloid	16.6	0.71061	29	3	-3.1	0.7		
			OBS 1a		dorsal spine	16.6		29	3	-3.0	0.7			
			OBS 2a		dorsal spine	16.3		29	3	-3.4	0.7			
			OBS 1b		dorsal spine	16.0		29	3	-3.6	0.7			
			OBS 2b		dorsal spine	16.7		29	3	-2.9	0.7			
			OBS 3b		dorsal spine	17.6		29	3	-2.1	0.7			
			OBS 4b		dorsal spine	17.4		29	3	-2.2	0.7			
			OBS 5b		dorsal spine	16.4		29	3	-3.3	0.7			
			Average of LBS3, LBS3A, LBS3B, OBS2A and OBS1B				15.9					-3.8		
			SD				0.3					0.3		
			Min				15.5					-4.1		
Max				16.3					-3.4					

**Table 2.**  $\delta^{18}\text{O}_\text{water}$  values and uncertainties calculated using a paleotemperature of  $29 \pm 3\%$  (Dera et al., 2009; Fischer et al., 2013), the  $\delta^{18}\text{O}_\text{P}$  values of shark teeth and spines (Fischer et al., 2013) preserved in the foreland Bourbon l'Archambault basin and the phosphate-water fractionation factor of Lécuyer et al. (2013). Grey lines indicate data used for paleoaltimetry reconstruction.